HHS Public Access

Author manuscript

ACS Appl Mater Interfaces. Author manuscript; available in PMC 2021 January 08.

Published in final edited form as:

ACS Appl Mater Interfaces. 2020 January 08; 12(1): 275–287. doi:10.1021/acsami.9b18624.

Intravital Vascular Phototheranostics and Real-Time Circulation Dynamics of Micro- and Nano-sized Erythrocyte-Derived Carriers

Wangcun Jia[†], **Joshua M. Burns**[#], **Betty Villantay**[†], **Jack C. Tang**[#], **Raviraj Vankayala**[⊥], **Ben Lertsakdadet**[†,‡], **Bernard Choi**[†,‡,▽], **J. Stuart Nelson**[†,‡], **Bahman Anvari**[#,*]

[†]Beckman Laser Institute and Medical Clinic, Department of Surgery, University of California, Irvine, Irvine, CA, 92617

[#] Department of Bioengineering, University of California, Riverside, Riverside, CA, 92521

[⊥]Radoptics LLC, Irvine, CA 92617

[‡]Department of Biomedical Engineering, University of California, Irvine, Irvine, CA, 92697

[▽]Edwards Life Sciences Center for Advanced Cardiovascular Technology, University of California, Irvine, Irvine, CA 92697

Abstract

Erythrocyte-based carriers can serve as theranostic platforms for delivery of imaging and therapeutic payloads. Engineering these carriers at micro- or nano-scales makes them potentially useful for broad clinical applications ranging from vascular diseases to tumor theranostics. Longevity of these carriers in circulation is important in delivering a sufficient amount of their payloads to the target. We have investigated the circulation dynamics of micro (~4.95 μm diameter) and nano (~91 nm diameter) erythrocyte-derived carriers in real time using near-infrared fluorescence imaging, and evaluated the effectiveness of such carrier systems in mediating photothermolysis of cutaneous vasculature in mice. Fluorescence emission half-lives of micro- and nano-sized carriers in response to a single intravenous injection were ~49 and ~15 minutes, respectively. A single injection of micro-sized carriers resulted in threefold increase in signal to noise ratio that remained nearly persistent over one hour of imaging time. Our results also suggest that a second injection of the carriers seven days later can induce a transient inflammatory response, as manifested by the apparent leakage of the carriers into the perivascular tissue. The administration of the carriers into the mice vasculature reduced the threshold laser fluence to

[*]**Corresponding Author** anvarib@ucr.edu.

AUTHOR CONTRIBUTIONS

All authors contributed to various aspects of the experimental design. J.M.B. fabricated and characterized the particles and contributed to the writing of the results section associated with such characterizations. W.J. and B.V. performed the animal experiments. J.C.T. performed the phosphatidylserine characterizations, assisted with particle fabrication and animal experiments. R.V. fabricated the particles to assess the effect of laser illumination time on fluorescence emission. B.L. and B.C. contributed to the animal model and imaging instruments. J.B. and J.C.T. contributed to the writing of the relevant parts of the methods section. B.A. and W.J. wrote the manuscript.

ASSOCIATED CONTENT

COMPETING INTERESTS

Authors B.A. and R.V. have a financial interest in Radoptics LLC, which is pursuing the commercial development of the particles reported in this manuscript. This interest did not interfere with the scientific work, judgment, and objectivity of the investigators in regards to the experimental procedures, analyses, reporting and interpretation of results, and any other aspect of the study.

All the remaining authors declare that they have no conflict of interest.

induce photothermolysis of blood vessels from >65 to 20 J/cm^2. We discuss the importance of membrane physicochemical and mechanical characteristics in engineering erythrocyte-derived carriers, and considerations for their clinical translation.

Keywords

cancer; erythrocyte engineering; delivery systems; laser dermatologic surgery; near-infrared imaging; phototherapy; port wine stain

INTRODUCTION

Theranostic carrier systems offer a capability for delivery of imaging and therapeutic payloads to sites of interest. These delivery systems are often introduced into the body through vasculature. Carriers on a micro-size scale normally remain confined to the vasculature and, as such, can be useful for the imaging and treatment of vascular disease. Nano-sized carriers with dimensions <200 nm are relevant for the delivery of imaging and/or therapeutic agents to tumors since such carriers can extravasate out of the vasculatures and accumulate at tumor sites by the enhanced permeability and retention effect resulting from leaky tumor vasculature and impaired lymphatic drainage.[1]

Various carrier systems such as polymeric particles,[2–3] liposomes,[4] genome-depleted brome mosaic virus,[5–6] and inorganic nanoplatforms[7] have been investigated.[8] For conventional non-stealth particles, opsonin proteins present in the blood serum bind to the particles, resulting in recognition and removal of the particles by the reticuloendothelial system and shortening their blood circulation time.[9] To address this issue, the surface of particles can be coated with polyethylene glycol (PEG).[10] PEGylation can prolong systemic circulation time of the particles to a certain degree and increase their accumulation in a tumor site to enhance imaging or therapeutic efficacy. However, studies have shown that repeated administration of PEGylated particles results in accelerated blood clearance due to the production of anti-PEG antibodies.[11–12] Moreover, dense and larger PEG chains hinder their interactions with the tumor microenvironment, inducing poor tumor penetration and uptake of particles.[13] Therefore, researchers have been motivated to explore other materials as carrier systems for theranostic applications.[14–15]

Erythrocytes are under extensive investigation as carrier systems for the delivery of various payloads including pharmaceutical agents, imaging probes, and photo-activated materials.[16–18] Key advantages of erythrocyte-based delivery systems are attributed to their potential biocompatibility and presence of specific membrane proteins, such as CD47 and decay-accelerating factor (CD55) that can impede phagocytosis and prolong circulation.[19] A particular feature of an erythrocyte-derived delivery platform is that their diameter can be engineered from micro- to nano-scale based on appropriate mechanical manipulation of erythrocytes, thereby providing a capability to develop a versatile platform for broad biomedical and clinical applications.[20]

A key issue pertaining to biomedical carrier systems, including those derived from erythrocytes, is their longevity within the vasculature. In the context of vasculature imaging

and phototherapeutics, the circulation lifetime of the carrier system determines the time window in which the vasculature can be imaged with sufficient contrast, or irradiated with sufficient absorption. In the context of cancer theranostics, increased circulation time of nano-carriers can result in greater accumulation of the carriers within the tumors, which can enhance the efficacy of imaging or therapy.[21] While normal erythrocytes have circulation times on the order of 3–4 months, to the best of our knowledge, real-time circulation dynamics of erythrocyte-derived optical carriers, particularly as related to their diameters, have not been previously reported in the literature. Herein, we report the first results on circulation dynamics of micro- and nano-sized erythrocyte-derived optical carriers based on real-time fluorescence imaging of the particles within the sub-dermal vasculature of healthy mice.

The erythrocyte-derived carriers in this study are doped with indocyanine green (ICG), currently the only near-infrared (NIR) absorbing dye approved by the United States Food and Drug Administration. ICG is an amphiphilic, water-soluble tricarbocyanine dye with a molecular mass of 775 Da. Since tissue autoflourescence emission is dramatically reduced in NIR spectral band (700–1700 nm), use of ICG can provide high signal-to-background ratio for biomedical imaging applications. Another inherent advantage of ICG is that the NIR light used to excite ICG can penetrate deeply into biological tissues (at least 1 cm depending on tissue type and wavelength) as there is minimal photon absorption and scattering by endogenous molecules.[22] Doping the erythrocyte-derived particles with ICG serves two important purposes. First, ICG is used as an optical tracer to fluorescently visualize the particles in real time. In doing so, time-dependent recordings of ICG fluorescence signal provides pertinent information applicable to circulation dynamics of erythrocyte-based delivery systems for various biomedical applications. Second, ICG itself can endow the particles with phototheranostic capability so that these particles can be used as materials for optical imaging and photo-therapeutic purposes.[18] When activated by absorption of an appropriate NIR wavelength, the particles can transduce the absorbed photon energy to emit light (e.g., fluorescence emission) or generate heat[18,23], or mediate production of reactive oxygen species.[18] We refer to these optical particles as NIR erythrocyte-derived transducers (NETs) as they can transduce the absorbed energy as described above. Another novel aspect of this study is that for the first time, we demonstrate that in addition to their vascular fluorescence imaging capability, NETs can also mediate photothermolysis of the vasculature in response to pulsed NIR laser irradiation, particularly at lower light fluences when compared to laser irradiation of the vasculature without exogenous chromophores. These results have relevance to the therapeutic utility of NETs by mediating photothermolysis of cutaneous capillary malformations known as port wine stains (PWSs).

Based on our in vivo real-time NIR fluorescence imaging results, we found that the average emission half-life of micro-sized NETs (μNETs, ~4.95 μm diameter) in response to a single retro-orbital injection was ~49 minutes, as compared to ~15 and 12 minutes for nano-sized NETs (nNETs, ~91 nm diameter) and free ICG, respectively. μNETs mediated threefold increase in signal-to-noise ratio (SNR) for blood vessels that remained nearly persistent over the one hour of imaging time post-injection. Furthermore, our imaging results suggest that the second injection of μNETs or nNETs seven days after the first injection induced a transient inflammatory response as manifested by apparent vasodilation and vascular

leakage of the contrast agent into the perivascular tissue. We discuss the physicochemical and biomechanical factors that are related to our findings. These factors are important for the engineering of a safe and effective erythrocyte-derived carrier platform for clinical translation.

RESULTS

Absorption, Fluorescence, and Diameter of NETs.

μNETs and nNETs suspended in 310 mOsm phosphate buffered saline (PBS) showed dominant peaks at 803 and 802 nm (Figure 1a), respectively, attributed to the monomeric form of ICG.[24] In comparison, the absorption spectrum of 18 μM free ICG dissolved in 310 mOsm PBS exhibited a dominant peak at 697 nm, which is attributed to the H-like aggregate form of ICG.[24] In response to photo-excitation at 785 nm, the fluorescence emission intensity values divided by the quantity of absorbed light (see Equation 1) were higher for NETs than that for free ICG up to ~855 nm (Figure 1b). Encapsulation-enhanced emission can be attributed to electrostatic interactions of amphipathic ICG molecules with NETs constituents (e.g., phospholipids, proteins) which hinder the mobility of ICG, thus reducing non-radiative relaxation from an excited electronic state. We have previously reported comprehensive characterization studies related to physical and optical properties of μNETs and nNETs.[24] These properties included ICG concentration-dependent zeta potentials, absorption and emission spectra, loading efficiency, excitation-emission maps, relative fluorescence quantum yield and photostability, are not repeated here. As an example, we point out that the spectrally-integrated fluorescence emissions of μNETs, and nNETs formed by mechanical extrusion, are not altered in a statistically significant manner when stored at 4 or 37 °C for up to 12 hours.[24]

The estimated mean peak hydrodynamic diameters of nNETs, as measured by dynamic light scattering (DLS), was ~91 nm (n = 4 measurements on each sample, Figure 1c). Lognormal fits to the DLS-based profiles yielded the mean peak ± standard deviation (SD) diameters of 93 ± 1 nm. In Figure 1d, we present a representative confocal microscopy image of μNETs. Based on the analysis of 30 μNETs from this image, the estimated mean ± SD diameters of μNETs were 4.95 ± 0.63 μm. The z-stack of the confocal images of μNETS (Figure S1, Supporting Information) further demonstrates that ICG was localized in both the interior core and membrane shell of μNETs.

Intravital fluorescence imaging of microvasculature using NETs as optical contrast agents.

Co-registration of a photographic image of mouse dermal microvasculature within the window chamber, obtained by white light illumination (Figure 2a), with a NIR fluorescence image mediated by μNETs (Figure 2b), demonstrates improved resolution to visualize both major and minor blood vessels attained by using μNETs. Dynamic angiography-like video in the first 37 s after injection of μNETs provides a clear presentation of the filling of μNETs in the vasculature (Video SI, Supporting Information). Representative dynamic changes in fluorescence intensity in the vasculature over the 60 minutes imaging period after μNETs injection is provided as Video S2, Supporting Information. A corresponding montage of the same imaging sequence is presented in Figure 2c.

Intravital fluorescent images of blood vessels in the window chamber at different time points after μNETs, nNETs, or free ICG administration are shown in Figure 3. The highest mean emission from blood vessels was observed at three minutes post injection for both μNETs and nNETs (Figures 3a, d), and at 47 seconds for free ICG (Figure 3g) (the region of interests (ROI) for measuring fluorescence intensity are illustrated by the yellow outlines in Figure S2, Supporting Information). The difference in the peak fluorescence time could be related to the different transit times of μNETs, nNETs and free ICG in arteries, veins, and capillaries. It also could be caused by the different elimination rates from the vasculature for the three agents. The maximum raw fluorescence intensity value for nNETs was significantly higher ($p<0.05$) than those for μNETs and free ICG (values of raw fluorescence intensity are provided in Figure S3, Supporting Information). At 30 minutes post-injection (Figures 3b, e), fluorescence intensity in the blood vessels was still high in response to either μNETs or nNETs administration, but very low at the same time after free ICG injection (Figure 3h). At 60 minutes post-injection (Figures 3c, f), blood vessels could still be clearly visualized in response to both μNETs and nNETs administration. However, blood vessels injected with free ICG (Figure 3i) were barely distinguishable from the background, thus confirming that free ICG was eliminated from the vasculature.

In vivo emission dynamics and quantitative fluorescence analysis.

Spatially-averaged emission intensities within the blood vessels (illustrated by yellow outlined ROIs in Figure S2, Supporting Information) from three animals were averaged first (Figure S4, Supporting Information). Normalized intensity values were calculated by dividing the raw fluorescence intensities in each ROI by the maximum value in the corresponding ROI. Average normalized values from three animals for each agent indicated that μNETs emission decayed more slowly as compared to those for nNETs and ICG (Figure 4a).

To obtain additional quantitative information from the fluorescent images associated with different agents, we determined the signal-to-noise ratio (SNR) between the blood vessels and the background noise in the perivascular tissue (see Equation 2). Mean SNR reached a maximum value of ~3 following injection of μNETs and remained nearly persistent with only 18% reduction at one hour post injection (Figure 4b). Maximum values of SNR associated with nNETs and free ICG were similar (~3.2) and were reduced by36 and 89%, respectively, at one hour post injection.

The emission half-life was calculated as the time when the normalized fluorescence intensity value in the ROI was reduced from 1 to 0.5 (Figure 4a). Specifically, half-lives for μNETs, nNETs, and ICG in the ROI were 49, 15, and 12 minutes, respectively. For μNETs and nNETs, the normalized intensity could be fitted with exponential functions (Figure S5, Supporting Information) using either one-phase decay (Figures S5a,c) or two phase decay models with smaller residuals (Figures S5b,d). However, for ICG, the normalized intensity curve could only be fitted with a two-phase decay model (Figure S5f, Supporting Information) but not a one-phase decay model (Figure S5e, Supporting Information). This difference implies that the elimination mechanisms for NETs or ICG are different.

In vivo emission dynamics of NETs in response to dual injection.

Seven days after the first injection, we confirmed that there was no remaining fluorescence in the blood vessels, and administered a second injection of μNETs or nNETs. While brightest emission was still observed at 3 minutes after the second injection of μNETs (Figure 5a), some glowing spots around capillary tips appeared as early as 10 minutes (Video S3, Supporting Information), pointed by white arrows in Figures 5b, e, f. We also studied dual-injection of μNETs fabricated from mice erythrocytes (n=3) in addition to those fabricated from bovine erythrocytes. Glowing spots around capillary tips were also observed after the second injection (Figure S6, Supporting Information). At later time points (30, and 60 minutes), bright stationary particles were observed in the main vessels and smaller vessels (Figures 5c–d). Besides stationary particles adherent to the vessel wall, there were also large particles flowing in the vessels that seemed to be aggregated μNETs (Video S4, Supporting Information). These stationary and flowing large particles disappeared from the vasculature 24 hours after the second injection. All animals receiving dual injections recovered without any apparent problem.

The average normalized fluorescence intensity (Figure 6a) associated with the second injection of μNETs (n=4 animals) decayed more slowly as compared to those associated with the single injection of μNETs (Figure 4a). The emission half-life in response to the second μNETs injection was longer than one hour (Figure 6a). However, the presence of highly fluorescent aggregates adherent to the vessel walls (Figure 5d and Video S4) could skew the measured fluorescence intensity towards a slower decay rate and consequently a longer emission half-life. While the same maximum value of SNR (~3) was reached after the second injection of μNETs, there was a more rapid decay in the SNR profile (Figure 6b). Reductions in SNR can be attributed to the presence of the glowing spots in the capillary regions (Figures 5e, f).

In response to the second injection of nNETs seven days after the initial injection, there was a progressive increase in background fluorescence (Figures 7a–c). Although, the fluorescence intensity in the ROIs was high, the image's SNR decayed substantially during the one hour time course after injection (Figure 7e). For the second injection of nNETs, the emission half-life was not consistent among the animals, ranging from 25 to >60 minutes (Figure 7d).

We also studied dual injection of ICG or injection of NETs following ICG injection and vice versa (Table S1, Supporting Information). Emission dynamics of the second ICG injection was nearly the same as the first ICG injection. Emission dynamics of the μNETs injection seven days following first ICG injection was similar to the first injection of μNETs.

NETs-mediated photothermolysis of blood vessels in conjunction with pulsed NIR laser irradiation.

We investigated the effectiveness of μNETs in mediating photothermolysis of the microvasculature using laser speckle contrast (LSC) imaging, which characterizes blood flow dynamics.[25] Without any exogenous agents, 755 nm pulsed laser irradiation (3 ms, 10 mm spot size) at a fluence as high as 65 J/cm^2 was insufficient to induce photothermolysis

of all the irradiated blood vessels (Figures 8a, c). Following retro-orbital administration of μNETS, blood vessels were irradiated at 100 s after injection, the time at which peak fluorescence intensity was approximately achieved. When the fluence was 20 J/cm^2, photothermolysis of most blood vessels occurred (Figures 8b, e). Fluence of 30 J/cm^2 was sufficient to induce photothermolysis of all the irradiated blood vessels (Figures 8c, f).

DISCUSSION

Encapsulation of imaging or therapeutic payloads into erythrocyte-derived carrier systems has gained increasing attention.[16,18–19] An important consideration in relation to these carriers is their longevity within the vasculature as it has relevance to the bioavailability of the encapsulated cargo for an intended clinical application. In this study, we investigated the vascular longevity of erythrocyte-derived carriers by real time fluorescence imaging, and utilized quantitative metrics (SNR) to assess the in vivo imaging capability of the carriers as a function of their diameters. We have also demonstrated the effectiveness of these carriers when doped with ICG in mediating photothermolysis of blood vessels. We discuss inter-related factors that can provide the mechanistic basis for our observations and guide further design and development of these particles for clinical translation. We also discuss the relevance of these particles to laser treatment of cutaneous capillary malformations.

Membrane physicochemical characteristics and role of phosphatidylserine in clearance of NETs.

The membrane bilayer of normal red blood cells (RBCs) is composed of phospholipids, cholesterol and an array of transmembrane proteins involved in transport, adhesion and signaling, as well as those defining the various blood group antigens.[26] Similar to other eukaryotic cells, the four major phospholipids of RBCs lipid bilayer are asymmetrically distributed where phosphatidylcholine and sphingomyelin are predominantly confined in the outer leaflet, whereas phosphatidylethanolamine and anionic phosphatidylserine (PS) are located in the inner leaflet. Localization of PS in the inner leaflet of normal RBCs is achieved by an ATP-dependent aminophospholipid translocase (flippase) that can rapidly shuttle PS from outer to inner leaflet. This activity is dependent on intracellular concentration of Ca^{+2}, and presumably associated with a P-type Mg^{2+}-ATPase[27] with ATP11C identified as a flippase.[28] Redistribution of PS to the external leaflet is considered as a hallmark of RBCs undergoing apoptosis, and their phagocytosis by macrophages, which contain PS receptors that recognize surface-exposed PS on apoptotic RBCs.[29–31] Furthermore, PS surface exposure is associated with removal of senescent normal RBCs by spleen macrophages.[32–33]

Our results indicate that the fractions of PS-positive, micro-sized erythrocyte ghosts (μEGs) and nano-sized EGs (nEGs) were comparable, and significantly higher than that for RBCs (Figure 9). This result suggests that display of PS on the outer leaflet can be induced by hypotonic treatment of RBCs,[34] and before the subsequent mechanical extrusion of hemoglobin-depleted μEGs to form nEGs. NETs with surface-exposed PS can then be recognized and engulfed by macrophages and, subsequently, removed from the vasculature.

In response to a single injection, nNETs have a lower average half-life in blood (~15 min) as compared to μNETs (~49 min) (Figures 4a, b). Since nearly the same fractions of μNETs and nNETs were PS-positive, the shorter half-life of nNETs in blood suggests that the removal rate of nNETs from the vasculature by macrophages is more efficient than the removal rate of μNETs. Given that the mean peak diameter of nNETs (~91 nm) is smaller than the average width of splenic interendothelial slits (~650 nm).[35] they can gain re-entry into the circulatory system; however, they can also be recognized by splenic macrophages within the cords of the red pulp (e.g., due to PS surface exposure), and subsequently removed from circulation. The shorter emission half-life of nNETs suggests that they may be more efficiently moved out of circulation by the spleen. The rate of a single phagocytosis event has been shown to be faster for engulfment of smaller particles, whereas large or irregularly shaped particles, such as μNETs, may be phagocytosed at a slower rate.[36] In a recent study of biodistribution of NETs in healthy Swiss Webster mice, we found that a statistically significant (p <0.05) higher level of nNETs (~26% of the injected amount per organ mass) were in mice spleens extracted 6 hours post injection, as compared to ~19% for μNETs.[37]

Both nNETs and μNETs with surface-exposed PS can also be recognized by Kupffer cells, macrophages adherent to the endothelial lining of liver sinusoids. Remaining nNETs escaping the liver Kupffer cells can then pass through the pores (~170 nm diameter[38]) between the fenestrated endothelial lining in liver sinusoids, extravasate into the space of Disse, and be eliminated from the body through the hepatobiliary mechanism, as mediated by hepatocytic uptake and subsequent secretion into the bile ducts.

While the mechanisms of NETs removal by macrophages remain to be fully understood, several factors influence the rate of the phagocytic activity induced by μNETs and nNETs. These factors include variations between the surface physicochemical characteristics of μNETs vs. nNETs such as differences in PS surface distribution, including the degree of PS spatial heterogeneities and surface density of exposed PS; differences in the presence and/or conformation of phagocytic impeding glycoproteins induced during fabrication (e.g., by mechanical extrusion to form nNETs) or possibly resulting from the greater surface curvature of nNETs; and differences in opsonization of μNETs and nNETs in terms of the conformation of the opsonized proteins on the surface of NETs due to surface curvature variations. One PS-binding opsonin is lactadherin (milk fat globule epidermal growth factor 8), a glycoprotein secreted by activated macrophages,[39] that binds to $\alpha_v\beta_3$ and $\alpha_v\beta_5$ integrins on macrophages and epithelial cells, respectively.[40–41] Lactadherin opsonization is also known to be size-dependent,[42] which may contribute to the difference between emission half-lives of NETs and nNETs.

Increased longevity of μNETs in blood vessels may be a resultant of their more effective localization to the vessel walls as compared to nNETs. It has been reported that particles with diameters <100 nm move with RBCs in the mainstream of the blood vessel lumen whereas larger particles (~1 μm diameter) tend to preferentially localize near the wall.[43] In another study, hydrogel particles with diameter of ~2 μm had enhanced margination to the wall when compared to particles with 500 nm diameters.[44] Hence, nNETs may move with RBCs in the mainstream of the vessel lumen whereas μNETs may be located in close

proximity to the endothelial cells, giving rise to increased longevity in the blood vessels and subsequently increased emission half-life.

The mechanisms underlying our observations with the second injection of NETs may be related to some type of induced "priming" effects in response to the first injection. One observation was the presence of bright stationary spots on the vessel wall (Figures 5c–d, Video S4, Supporting Information) and glowing regions around the capillary tips (Figures 5b, e, f, Video S3, Supporting Information) after the second injection of μNETs. RBCs (and potentially NETs) with surface-exposed PS can bind to PS receptors on the endothelial cells of the vasculature.[45–46] These receptors include $\alpha_V\beta_3$ integrins and CD36,[47] and CXCL16,[48] a chemokine that can also be present as a transmembrane protein to act as a scavenger receptor and bind to PS. It has been demonstrated that both the PS receptor mRNA and the receptor levels in endothelial cells reach their respective maximum values at 4 and 6 hours in response to interleukin (IL)-lα induced activation in vitro.[46] Binding of PS-exposed RBCs to the endothelial PS receptor has also been reported as a basis for the adhesion of RBCs to the endothelium of the central retinal vein.[49] Lactadherin-mediated phagocytosis of PS-exposed RBCs by endothelial cells through the α_V integrin pathway has been indicated.[50]

After the first injection of NETs, the endothelial cells may be primed in a way to interact more effectively with the PS on the surface of the second-injected NETs through the activated PS receptors. Although it is not known if the first injection of NETs with PS surface exposure can induce up-regulation of the PS receptor mRNA and expression of the receptor on endothelial cells, it may represent a priming effect, leading to binding of the NETs to endothelial cells upon the second injection which is manifested by the adherent fluorescent particles to the vessel wall and the glowing regions around the capillary tips. Other types of priming effects resulting from the first injection of NETs may lead to the production of cytokines, including tumor necrosis factor (TNF)-α by macrophages, and activation of the complement system such as the production of C3a and C5a fragments to cause dilation of small blood vessels after the second injection of NETs. Such dilated small vessels could accommodate the μNETs, a mechanism consistent with the observed glows from the capillary regions in Figures 5b, e, f. The priming responses may also represent a sensitization effect that involves the production of immunoglobulin E (IgE) after the first injection of NETs. The second injection may subsequently trigger the activation of IgE binding cells, such as basophils and mast cells.

Another observation was the increase in fluorescence emission from perivascular areas after the second injection of nNETs (Figures 7b, c). These results seem to suggest that there was extravasation of nNETs from the microvasculature after its second injection. Increased permeability of blood vessels, leading to vascular leakage, is associated with an inflammatory response and may have been induced by a priming effect after the first injection of nNETs. Cytokines, such as TNF-α, IL1, and IL6, released during inflammation act on endothelial cells, leading to increased vascular permeability.[51] Vascular endothelial growth factor (VEGF) is also a contributor to increased vascular permeability by uncoupling endothelial cell-cell junctions and inducing endothelial fenestrations.[52–53] Several growth factors, including epidermal growth factor and transforming growth factor-α can upregulate

VEGF mRNA expression. Additionally, inflammatory cytokines, such as ILl-α and IL-6, can induce the expression of VEGF in various cell types.[54]

The integrity of endothelial cell-cell junction is regulated by the adherens, tight, and gap junctions comprised of different adhesion molecules.[55] At adherens junctions, the VEGFR2 receptor associates with vascular endothelial (VE)-cadherin to regulate the cell-cell junction integrity and provide a mechanism for VEGF-mediated vascular disruption.[52] It has been demonstrated that Src family protein tyrosine kinases are required for VEGF-induced phosphorylation of adherens junctions proteins, which leads to vascular leakage in vivo.[52] Once these paracellular pathways have become leaky, nNETs with diameters on the order of ~91 nm can extravasate out of the vasculature through the induced endothelial gaps as compared to μnets with substantially larger diameters (~4.95 μm diameter). Leakage of negatively-charged mecaptoundeonic acid-capped silver nanoparticles after a single injection[56] and titanium dioxide nanoparticles following repeated injections in mice have been reported.[57]

Biomechanical characteristics.

Normal RBCs are highly deformable structures. The discoid biconcave shape of normal RBCs endows them with a high surface-to-volume ratio (~1.5) and facilitates remarkable reversible deformations that allows their repeated passages through narrow capillaries as they transverse from the splenic cord to splenic sinus without significant changes in their surface area. The excess surface area (~40% higher than a sphere of the same volume), coupled with the structural organization of normal RBCs, are the key determinants of the mechanical characteristics of RBCs. The strong adhesion between the membrane bilayer and the cytoskeleton is essential in maintaining the membrane surface area. This adhesion is provided by the linkages between the intracellular domains of membrane proteins and spectrin-based cytoskeleton network.[26] Particularly important linkages are provided by membrane proteins Band and RhAG that link to the spectrin network via Ankyrin, and glycophorin C, XK, Rh, and Duffy, which provide the linkage via protein 4.1R.[58–59] Binding of PS to cytoskeletal proteins and the spectrin network is also an important contributor to the mechanical stability and deformability of normal RBCs.[60–61]

Rupturing the PS linkages to cytoskeletal proteins, in addition to structural changes in the spectrin network, may occur during the mechanical extrusion steps when fabricating the nNETs. It is possible that such physical changes to the architecture of nNETs may alter their mechanical properties. However, in comparison to PS surface exposure as a mechanism for removal of nNETs from the vasculature, the mechanical characteristics of nNETs may not play a major role in their circulation dynamics since nNETs are sufficiently small to pass through splenic interendothelial slits and be re-introduced into circulation (if escaping the splenic macrophage cells).

For μNETs, their mechanical properties and induced sphericity can play an impactful role in influencing their circulation dynamics. Loss of membrane surface area and the resulting shape change from discoids to spheres compromises the ability of μNETs to effectively transverse through the splenic slits so that they may become trapped within the cords and phagocytosed by macrophages.[62] The resultant shape change of μNETs also implies that

structural changes to the spectrin network as well as membrane-cytoskeletal adhesion could occur which ultimately affect the mechanical characteristics of μNETs. In a recent study, we reported that the membrane stiffness of μNETs is higher than that of RBCs by about 28% −62%,[63] therefore, indicating a reduction in deformation capability of μNETs for effective splenic passage.

While the depletion of hemoglobin from RBCs during the formation of μNETs can contribute to the resulting shape changes, the ensuing mechanical changes are likely not a contributing factor in influencing the longevity of μNETs in circulation as compared to PS-mediated removal that results from the hypotonic treatment of RBCs. Cytoplasmic viscosity of RBCs increases with increased levels of intracellular hemoglobin concentration,[64–65] hence, reducing the deformation capability of RBSs. However, in the case of μNETs, a reduction in cytoplasmic viscosity is actually expected due to hemoglobin depletion.

The various factors described above, including PS surface exposure, changes in shape, lowered surface-to-volume ratio, reduced deformability and increased membrane stiffness, can possibly induce prothrombotic effects by NETs. In particular, in response to the second injection of μNETs, we observed bright particles flowing in the vessels that appeared to be aggregated (Video S4, Supporting Information). These aggregates may be a composite of μNETs and platelets. Formation of μNETs aggregates is consistent with the reported formation of stacked rouleaux of RBCs.[66] While the mechanisms of RBC rouleaux formation is not fully understood, proposed mechanisms that may also be relevant to NETs, including the role of specific plasma proteins (particularly fibrinogen) adsorbed on adjacent RBCs to mediate bridging of the RBCs,[67] or conversely, a lower localized protein concentration near the surface of RBCs (as compared to the surrounding medium), leading to an osmotic gradient and attractive forces.[68] Since the formation of RBCs rouleaux is reversible as the shear rate increases, it is also possible that a similar reversible process takes place with μNETs aggregates. In the course of our study, the observed μNETs aggregates disappeared within 24 hours after injection.

In relation to toxicological assessment of NETs, results of our recent study in Swiss Webster mice indicated that values of various hematological profiles (including white blood cell count, RBC count, platelets, hemoglobin, and hematocrit) at 24 hours post-injection of μNETs or nNETs were either within the normal range or not changed in a statistically significant manner.[37] Similarly, there were no statistically significant changes in levels of alanine aminotransferase and aspartate aminotransferase, enzymes associated with liver function, or any changes in levels of urea nitrogen and creatinine associated with kidney function. Furthermore, histological analysis of various organs (heart, liver, spleen, lung, and kidney) did not show any pathological alterations.

Example of clinical application and outlook.

A particular application of μNETs relates to laser treatment of port wine stain (PWS) birthmarks. PWSs are currently treated by laser irradiation using visible wavelengths in the range of 585–595 nm which are preferentially absorbed by hemoglobin, an endogenous chromophore in blood. Conversion of the absorbed light to heat causes thermal damage to the blood vessels and subsequent PWS clearance. However, melanin within the melanocytes,

located in the basal epidermal layer of skin and residing over the abnormal plexus of dermal capillaries, has a relatively strong optical absorption over the current laser treatment spectral band. As such, photons intended to reach the dermal vasculature are partially absorbed within the epidermis. The outcome can be non-specific thermal injury to the epidermis and insufficient heat generation within the vasculature to provide an adequate treatment.

An alternative phototherapeutic approach can potentially be developed by using NIR wavelengths in conjunction with intravascular administration of μNETs. For example, by changing the treatment wavelength from 585 to 755 nm, a nearly threefold reduction in the absorption coefficient of a single melanosome can be achieved.[69] This approach offers several advantages: (1) reduced risk of non-specific thermal injury to the epidermis to potentially allow treatment of individuals with moderate to heavy pigmentation;[70] (2) increased depth of optical penetration to reach deeply-seated blood vessels (e.g., > 500 μm below the skin surface);[70] and (3) heat generation within the blood vessels resulting from the absorption of lCG within μNETs to induce photothermolysis of the abnormal vasculature plexus. Our results demonstrate that by encapsulating ICG within μNETs, its retention time within the vasculature is prolonged (~12 minutes half-life for free ICG vs ~49 minutes for μNETs). Therefore, μNETs can potentially extend the therapeutic window of time during which laser therapy of PWS can be performed, as compared to free ICG.

In consideration of the aforementioned physicochemical and biomechanical factors associated with NETs, it is important that these factors are taken into account during the fabrication process of erythrocyte-derived carriers with the aim of not only prolonging the retention time of the particles within the vasculature but also overcoming potentially adverse effects. As suggested by our imaging results, the second injection of erythrocyte-derived carriers after one week following the first injection can lead to an inflammatory response. Therefore, adequate injection interval protocols, as well as fabrication protocols, need to be developed to avoid undesirable inflammatory responses.

CONCLUSION

We have investigated the circulation dynamics of micron and nano-sized erythrocyte-derived carriers in real time by near infrared fluorescence imaging of mice vasculature. The average emission half-lives of micro- and nano-sized carriers in blood vessels in response to a single intravenous injection were ~49 and 15 minutes, respectively. Second injection of the particles seven days after the first injection increased the average emission half-life to > 1 hour for microsized, with variable half-life ranging from ~25 minutes to >60 minutes for nano-sized carriers. Surface exposure of phosphatidylserine on the surface of these carriers can be an important mechanism for their removal from circulation. The shorter emission half-life of the nano-sized particles in blood after the first injection suggests that macrophages may be more efficient in removal of these particles when mediated through a phosphatidylserine surface exposure mechanism. Shape and deformation characteristics of micro-sized carriers can also contribute to the circulation time of these particles. Such biochemical and biomechanical characteristics are important considerations towards the engineering of erythrocyte-derived platforms for clinical translation in a safe and effective manner.

MATERIALS AND METHODS

Fabrication of NETs.

Erythrocytes were separated from bovine whole blood (Rockland Immunochemicals, Inc., Limerick, PA) by centrifugation (l,300xg, 5 minutes, 4 °C) and the plasma and buffy coat were discarded. Isolated erythrocytes were washed twice with 310 mOsm phosphate buffer saline (PBS) (referred to as the 1X solution) (pH ~8.0), and then subjected to hypotonic treatment using 0.25XPBS (80 mOsm, pH ~8.0) and centrifuged (20,000xg, 15 minutes, 4 ^{0}C). This process was repeated until an opaque pellet containing micro-sized hemoglobin-depleted erythrocyte ghosts (EGs) was formed. To obtain nano-sized EGs (nEGs), the micro-sized EGs (μEGs) were extruded 40 times through 400 nm polycarbonate porous membranes (Track-Etched Membranes, Whatman, Florham Park, NY), followed by 40 more extrusions through 200 nm polycarbonate membranes, and another 40 times through 100 nm polycarbonate membranes using an Avanti mini extruder (Avanti Polar Lipids, Inc., Alabaster, AL).

We concentrated the μEGs and nEGs 10 times by centrifugation (20,000xg, 15 minutes, 4 °C for μNETs; 98,800xg, 1 hour, 4 °C for nNETs) and re-suspended the EGs pellet in 1 ml of 1X PBS. To form μNETs or nNETs, 1 ml of concentrated μEGs or nEGs were incubated in loading buffer consisting of 3 ml of 2.58 mM free ICG dissolved in water and 3 ml of hypotonic buffer ($Na_2HPO_4/Na_2H_2PO_4$, 140 mOsm, pH ~5.8) for 10 minutes (final ICG concentration in loading buffer ~1.11 mM). After incubation, the resulting NETs suspensions were centrifuged (20,000xg, 15 minutes, 4°C for μNETs; 74,000xg, 30 minutes, 4 °C for nNETs) and supernatants were removed. The pellets were washed two more times using 1X PBS to remove any remaining non-encapsulated ICG, and the final μNETs and nNETs were suspended in 1XPBS and stored at 4°C in the dark.

Characterization of NETs.

Absorption spectra of NETs and 18 μM free ICG suspended in 1X PBS were obtained using a UV-visible spectrophotometer (Cary 50 UV-Vis spectrophotometer, Agilent Technologies, Santa Clara, CA) with an optical path length of 1 cm. To avoid saturation in measurements of NIR absorbance values during spectral recordings, solutions of μNETs and nNETs were further diluted by a factor of 100 using 1XPBS.

Fluorescence emission spectra of NETs and 6.5 μM free ICG in 1X PBS were acquired in response to 785±2.5 nm excitation with a 450W xenon lamp and recorded over the 820 – 870 nm spectral band using a fluorimeter (Fluorolog-3 spectrofluorometer, Edison, NJ). Fluorescence emission spectra (χ) scaled to the quantity of the absorbed light were determined as:

$$\chi(\lambda) = \frac{[F(\lambda)]}{\left[1 - 10^{-A\left(\lambda_{ex}\right)}\right]} \quad (1)$$

where A and F are the wavelength (λ) dependent absorbance and intensity of the emitted fluorescence light, respectively, and λ_{ex} is the excitation wavelength. Hydrodynamic

diameters of NETs suspended in 310 mOsm PBS was measured by dynamic light scattering (Zetasizer NanoZS90, Malvern Instruments Ltd, Malvern, United Kingdom).

Confocal Microscopy of μNETs.

A small suspension of μNETs in 1X PBS was seeded on poly-l-lysine coated slides and imaged using a confocal microscope (Zeiss LSM 510, Carl Zeiss, Inc., USA). Samples were photo-excited at 633 nm, and fluorescence emissions greater than 650 nm were collected. We present falsely colored microscopic images of the ICG fluorescence emission (red channel).

Phosphatidylserine characterization by flow cytometry.

RBCs, μEGs and nEGs were assayed for PS exposure using annexin V labeled with Alexa Fluor488 (AF488) (Invitrogen, Carlsbad, CA). Prior to analysis, each sample was incubated for 30 minutes at room temperature with annexin V conjugate in the presence of a binding buffer, which contained 10 mM HEPES, 140 mM NaCl, and 2.5 mM $CaCl_2$ (pH 7.4). Fluorescence was measured using a BD LSRII flow cytometer (excitation laser: 488 nm, emission filter: 515–545 nm), and the PS-positive populations were quantified using FlowJo V10.

Animal model.

All experiments were conducted under a protocol approved by the Institutional Animal Care and Use Committee, University of California, Irvine (Protocol number AUP-17–074). We implanted a dorsal skinfold window chamber on male mice (25–30 g, C3H strain). Details of the chamber structure and surgical procedure can be found elsewhere.[71] In brief, a mouse was anesthetized with a combination of ketamine and xylazine (2:1 ratio, 0.1/100 g body weight) administered by intraperitoneal injection. A pair of thin titanium window frames (0.4 mm in thickness) was attached to the front and back sides of a dorsal skinfold with 3 screws of 1.5 mm in diameter and 2 sutures. The front layer of the skinfold within the 10 mm circular observation window was removed to expose the subdermal blood vessels in the back layer of the dorsal skinfold, which was kept intact to minimize inflammations in the imaging area. Sterile isotonic saline solution was applied onto the exposed skin, followed by placement of a glass cover slip and a retention ring to seal the chamber and protect the subdermis from dehydration and contamination.

The animal was allowed to recover from anesthesia and surgery on a heating pad. One day after placement of the window chamber, the animal was anesthetized using a mixture of oxygen and 1.5% isoflurane. This method allows a consistent level of anesthesia during the experiment as compared to injection of ketamine and xylazine. The mouse was then placed on the translational stage of an inverted fluorescence microscope (see next subsection for details). Once the animal's body temperature, measured with an NIR thermometer, and respiratory rate were stabilized, a 150μL ICG solution or NETs suspension was delivered via retro-orbital injection using a 27.5-gauge insulin syringe. Recording of fluorescence images from the window chamber started immediately before the retro-orbital injection.

This model permits in vivo longitudinal visualization of blood flow dynamics in sub-dermal blood vessels.[72–73] It also allows direct determination of the circulation dynamics of a carrier system in blood, such as NETs, in real time without sacrificing the animals at a given time point post-injection. The blood vessels in the window remain visible over an extended time, on the order of two weeks. Therefore, the same animal can be used repeatedly for multiple injections after the injected substance is cleared to minimize data variability when different animals are used.

In vivo fluorescence imaging.

The experimental setup used to record the fluorescence emission from either free ICG or NETs circulating in the vasculature included a custom-built microscopy system consisting of: (1) an inverted microscope (Diaphot, Nikon Instruments, Melville, NY); (2) an EMCCD camera (QuantEM 512SC, Photometries, Tucson, AZ); (3) a filter set (49030 ET-INDO GR, Chroma Technology, Bellows Falls, VT); and (4) a 785 nm diode laser (BWF-785–450E, B & W Tek, Newark, DE) with a maximum power of 500 mW. The laser beam was expanded to a 25 mm diameter spot on the window chamber and the optical intensity was 0.1 W/cm^2. The filter set passed emission wavelengths between 815 and 845 nm. The animal was placed on a layer of insulation material on the microscope stage, and an air stream incubator (ASI 400, Nevtek, Williamsville VA) was used to maintain the normal body temperature at 37±1°C. A customized fixture with two metal plates was used to hold the window chamber on the translational stage. The dermal side of the window faced the objective lens and the epidermal side was illuminated with the laser beam.

Fluorescence images were acquired over an interval of 60 minutes. During the first 5 minutes, images were acquired every second in order to capture the rapid changes in fluorescence intensity. During the next 10 minutes, image acquisition interval was every minute. During the final 45 minutes, images were acquired every five minutes. Spatially-averaged fluorescent intensity in the blood vessels (shown as regions of interest (ROI) enclosed by yellow outlines in Figure S2, Supporting Information), and the area surrounding the blood vessels within the window chamber were quantified using ImageJ. To trace blood vessels, a fluorescence image was first analyzed by ImageJ's "Tubeness" plug-in which produces an intermediate image showing how "tube-like" each point in the original image is.[74] Then a threshold was applied to the "Tubeness" image to select most of the blood vessels in the image and convert to blood vessel ROI. ROI for the surrounding tissue was created by inverting the blood vessel ROI. To evaluate image quality, we quantified the signal-to-noise ratio (*SNR*) by the following expression:

$$\mathrm{SNR} = \frac{I_{\mathrm{BV}} - I_{\mathrm{T}}}{\sigma_{\mathrm{T}}}$$

where I_{BV} is the mean fluorescence intensity in the blood vessels, I_{T} is the mean fluorescence intensity in tissue surrounding the blood vessels, and σ_{T} is the standard deviation of fluorescence intensity in the tissue surrounding the blood vessels.

The diode laser was kept on during the initial 5 minutes of imaging and the window skin temperature was monitored with an infrared camera (A325sc, FLIR, Nashua, NH). The average skin temperature in the window increased slightly from 35.2°C to 35.7°C after 5 minutes of continuous illumination. When the imaging interval was one or five minutes, the diode laser was blocked between each image acquisition to avoid potential skin heating or ICG photobleaching. The total time of laser illumination was approximately 6 minutes. We performed an experiment to confirm that this total time of laser illumination, accumulated intermittently over the course of an experiment, had a negligible effect on the fluorescence intensity (Figure S7, Supporting Information). However, our previous study shows that 3 minutes of cyclic laser irradiation at a much higher intensity (19.7 W/cm^2), as compared to the intensity of 0.1 W/cm^2 used in this study, can result in photo-degradation of NETs.[23]

Since the window chamber model allows imaging of the blood vessels over a two weeks period, a single mouse can be used for multiple injections of different or same type of agents. The left or right retro-orbital sinus was used alternatively. Before each injection, a background fluorescence image was recorded to confirm that previously injected fluorophores were eliminated from blood circulation. The injection scheme used in this study is shown in Table S1, Supporting Information. For the images corresponding to dual injection of μNETs (Figure 5), window chambers were installed on the mouse one day before the second injection. For all other animals receiving two or more injections, window chambers were installed on the mouse one day before the first injection.

Laser irradiation of the microvasculature.

Laser irradiation was performed on the window (subdermal) side of the preparation. The animal was anesthetized using a mixture of 1.5% isoflurane and oxygen. After anesthesia, blood flow maps were acquired by laser speckle contrast (LSC) imaging, followed by 150 μL injection of μNETs into the retro-orbital sinus for the laser+μNETs group. At 100 seconds post injection, blood vessels were irradiated with an alexandrite laser (GentleLASE, Candela Corp, Wayland, MA) at a wavelength of 755 nm and pulse duration of 3 ms. The spot size was 10 mm which covered the entire window. Only one laser pulse was delivered to irradiate the blood vessels in the window. For the laser-only group, laser irradiation was performed after blood flow maps were obtained by LSC imaging. Laser pulse energies were measured using an energy meter (FL250A-SH with Nova display, Ophir, Logan, UT).

LSC imaging was used to determine blood flow dynamics in the window before and ~5 minutes after laser irradiation. During this imaging procedure, the window was trans-illuminated with a continuous wave HeNe laser (632.8 nm, 30 mW), and the resulting speckle pattern produced by the interference of the light waves that scatter from various tissue and blood components in the window was imaged by a CCD camera (10 ms integration time). When blood flow is present, speckle pattern varies with time, resulting in areas of low contrast in the time-integrated images; otherwise, the speckle pattern is static and contrast is high. Ten speckle images were collected, and the contrast was calculated with a sliding-window-based algorithm.[75] Average contrast was converted to a blood flow index map.[76]

Supplementary Material

Refer to Web version on PubMed Central for supplementary material.

ACKNOWLEDGEMENTS

This study was supported in part by grants from the National Institute of Arthritis and Musculoskeletal and Skin Diseases (R01-AR068067) and the U. S. National Science Foundation (CBET-1509218). Institutional support from the LAMMP program (NIH: P41EB015890), Beckman Laser Institute Endowment, and the David and Lucile Packard Foundation are also acknowledged.

ABBREVIATIONS

AF488	Alexa Fluor488
CCD	charge-coupled devices
CD47	cluster of differentiation 47
CD55	decay-accelerating factor
CR1	complement receptor type 1
DLS	dynamic light scattering
EGs	erythrocyte ghosts
μEGs	micro-sized erythrocyte ghosts
nEGs	nano-sized EGs
EMCCD	electron multiplying charge-coupled devices
ICG	indocyanine green
IgE	immunoglobulin E
IL-1	interleukin 1
IL-6	interleukin 6
LSC	laser speckle contrast
NIR	near-infrared
NETs	NIR erythrocyte-derived transducers
μNETs	micro-sized NETs
nNETs	nano-sized NETs
PBS	phosphate buffered saline
PS	phosphatidylserine
PWSs	port wine stains

RBCs	red blood cells
RhAG	Rh-associated glycoprotein
ROI	regions of interest
SD	standard deviation
SNR	signal-to-noise ratio
TNF	tumor necrosis factor
VEFG	Vascular endothelial growth factor
VEGFR2	VEFG receptor 2

REFERENCES

(1). Peer D; Karp JM; Hong S; FaroKhzad OC; Margalit R; Langer R Nanocarriers as an Emerging Platform for Cancer Therapy. Nat. Nanotechnol. 2007, 2 (12), 751–760, DOI: 10.1038/nnano.2007.387. [PubMed: 18654426]

(2). Saxena V; Sadoqi M; Shao J Enhanced Photo-Stability, Thermal-Stability and Aqueous-Stability of Indocyanine Green in Polymeric Nanoparticulate Systems. J. Photochem. Photobiol. B, Biol. 2004, 74 (1), 29–38, DOI: 10.1016/j.jphotobiol.2004.01.002.

(3). Yu J; Javier D; Yaseen MA; Nitin N; Richards-Kortum R; Anvari B; Wong MS Self-Assembly Synthesis, Tumor Cell Targeting, and Photothermal Capabilities of Antibody-Coated Indocyanine Green Nanocapsules. JACS 2010, 132 (6), 1929–1938, DOI: 10.1021/ja908139y.

(4). Shemesh CS; Moshkelani D; Zhang H Thermosensitive Liposome Formulated Indocyanine Green for Near-Infrared Triggered Photodynamic Therapy: In Vivo Evaluation for Triple-Negative Breast Cancer. Pharm. Res. 2015, 32 (5), 1604–1614, DOI: 10.1007/s11095-014-1560-7. [PubMed: 25407543]

(5). Guerrero Y; Singh SP; Mai T; Murali RK; Tanikella L; Zahedi A; Kundra V; Anvari B Optical Characteristics and Tumor Imaging Capabilities of Near Infrared Dyes in Free and Nano-Encapsulated Formulations Comprised of Viral Capsids. ACS Appl.Mater. Interfaces 2017, 9(23), 19601–19611, DOI: 10.1021/acsami.7b03373. [PubMed: 28524652]

(6). Jung BS; Rao ALN; Anvari B Optical Nano-Constructs Composed of Genome-Depleted Brome Mosaic Virus Doped with a Near Infrared Chromophore for Potential Biomedical Applications. ACSNano 2011, 5 (2), 1243–1252, DOI: 10.1021/nnl028696.

(7). Sheng Z; Hu D; Xue M; He M; Gong P; Cai L Indocyanine Green Nanoparticles for Theranostic Applications. Nano-MicroLetters 2013, 5 (3), 145–150, DOI: 10.5101/nml.v5i3.

(8). Zhu HJ; Cheng PH; Chen P; Pu KY Recent Progress in the Development of Near-Infrared Organic Photothermal and Photodynamic Nanotherapeutics. Biomater. Sci. 2018, 6 (4), 746–765, DOI: 10.1039/c7bm01210a. [PubMed: 29485662]

(9). Emsting MJ; Murakami M; Roy a.; Li S-D Factors Controlling the Pharmacokinetics, Biodistribution and Intratumoral Penetration of Nanoparticles. J. Controlled Release 2013, 172 (3), 782–794, DOI: 10.1016/j.jconrel.2013.09.013.

(10). Jokerst JV; Lobovkina T; Zare RN; Gambhir SS Nanoparticle PEGylation for imaging andtherapy. Nanomedicine 2011, 6 (4), 715–728, DOI: 10.2217/nnm.11.l9. [PubMed: 21718180]

(11). ishida T; Maeda R; Ichihara M; Irimura K; Kiwada H Accelerated Clearance of Pegylated Liposomes in Rats after Repeated Injections. J. Controlled Release 2003,88 (1), 35–42, DOI: 10.1016/s0168-3659(02)00462-5.

(12). Armstrong JK; Hempel G; Koling S; Chan LS; Fisher T; Meiselman HJ; Garratty G Antibody Against Poly(Ethylene Glycol) Adversely Affects Peg-Asparaginase Therapy in Acute Lymphoblastic Leukemia Patients. Cancer 2007, 110 (1), 103–111, DOI: 10.1002/cncr.22739. [PubMed: 17516438]

(13). Yoo J-W; Chambers E; Mitragotri S Factors that Control the Circulation Time of Nanoparticles in Blood: Challenges, Solutions and Future Prospects. Curr. Pharm. Des. 2010,16 (21), 2298–2307. [PubMed: 20618151]

(14). Li JC; Zhen X; Lyu Y; Jiang YY; Huang JG; Pu KY Cell Membrane Coated Semiconducting Polymer Nanoparticles for Enhanced Multimodal Cancer Phototheranostics. ACS Nano 2018,12 (8), 8520–8530, DOI: 10.1021/acsnano.8b04066. [PubMed: 30071159]

(15). Zhen X; Cheng PH; Pu KY Recent Advances in Cell Membrane-Camouflaged Nanoparticles for Cancer Phototherapy. Small 2019,15 (1), DOI: 10.1002/Smll.201804105.

(16). Muzykantov VR Drug Delivery by Red Blood Cells: Vascular Carriers Designed by Mother Nature. Expert Opin. DrugDel. 2010, 7 (4), 403–427, DOI: 10.1517/17425241003610633.

(17). Antonelli A; Magnani M Red Blood Cells as Carriers of Iron Oxide-Based Contrast Agents for Diagnostic Applications. J. Biomed. Nanotechnol. 2014, 10 (9), 1732–1750, DOI: 10.1166/jbn.2014.1916. [PubMed: 25992439]

(18). Bums JM; Vankayala R; Mac JT; Anvari B Erythrocyte-Derived Theranostic Nanoplatforms for Near Infrared Fluorescence Imaging and Photodestruction of Tumors. ACS Appl.Mater. Interfaces 2018,10 (33), 27621–27630, DOI: 10.1021/acsami.8b08005. [PubMed: 30036031]

(19). Villa CH; Anselmo AC; Mitragotri S; Muzykantov V Red Blood Cells: Supercarriers for Drugs, Biologicals, and Nanoparticles and Inspiration for Advanced Delivery Systems. Adv. DrugDelivery Rev. 2016,106, 88–103, DOI: 10.1016/j.addr.2016.02.007.

(20). Burns JM; Saager R; Majaron B; Jia W; Anvari B Optical Properties of Biomimetic Probes Engineered from Erythrocytes. Nanotechnology 2017,28 (3), 035101, DOI: 10.1088/1361-6528/28/3/035101. [PubMed: 27966473]

(21). Duan XP; Li YP Physicochemical Characteristics of Nanoparticles Affect Circulation, Biodistribution, Cellular Internalization, and Trafficking. Small 2013, 9 (9–10), 1521–1532, DOI: 10.1002/smll.201201390. [PubMed: 23019091]

(22). Hong G; Antaris AL; Dai H Near-Infrared Fluorophores for Biomedical Imaging. Nat. Biomed. Eng. 2017,1, 0010, DOI: 10.1038/s41551-016-0010.

(23). Bahmani B; Bacon D; Anvari B Erythrocyte-Derived Photo-Theranostic Agents: Hybrid Nano-Vesicles Containing Indocyanine Green for Near Infrared Imaging and Therapeutic Applications. Sci. Rep. 2013, 3, 2180, DOI: 10.1038/Srep02180. [PubMed: 23846447]

(24). Tang JC; Partono A; Anvari B Near-Infrared-Fluorescent Erythrocyte-Mimicking Particles: Physical and Optical Characteristics. IEEE Trans. Biomed. Eng. 2019, 66 (4), 1034–1044, DOI: 10.1109/Tbme.2018.2866368. [PubMed: 30130175]

(25). Choi B; Kang NM; Nelson JS Laser speckle imaging for monitoring blood flow dynamics in the in vivo rodent dorsal skin fold model. Microvasc. Res. 2004, 68 (2), 143–146, DOI: 10.1016/j.mvr.2004.04.003. [PubMed: 15313124]

(26). Mohandas N; Gallagher PG Red Cell Membrane: Past, Present, and Future. Blood 2008, 112 (10), 3939–3948, DOI: 10.1182/blood-2008-07-161166. [PubMed: 18988878]

(27). Daleke DL Regulation of Phospholipid Asymmetry in the Erythrocyte Membrane. Curr. Opin. Hematol. 2008,15 (3), 191–5, DOI: 10.1097/MOH.0b013e3282f97af7. [PubMed: 18391783]

(28). Arashiki N; Takakuwa Y; Mohandas N; Hale J; Yoshida K; Ogura H; Utsugisawa T; Ohga S; Miyano S; Ogawa S; Kojima S; Kanno H ATP11C is a Major Flippase in Human Erythrocytes and Its Defect Causes Congenital Hemolytic Anemia. Haematologica 2016,101 (5), 559–565, DOI: 10.3324/haematol.2016.142273. [PubMed: 26944472]

(29). Zwaal RF; Comfurius P; Bevers EM Surface Exposure of Phosphatidylserine in Pathological Cells. Cell.Mol. Life Sci. 2005, 62 (9), 971–88, DOI: 10.1007/s00018-005-4527-3. [PubMed: 15761668]

(30). Fadok VA; Bratton DL; Rose DM; Pearson A; Ezekewitz RAB; Henson PM A Receptor for Phosphatidylserine-Specific Clearance of Apoptotic Cells. Nature 2000, 405, 85, DOI: 10.1038/35011084. [PubMed: 10811223]

(31). Devitt A; Moffatt OD; Raykundalia C; Capra JD; Simmons DL; Gregory CD Human Cd14 Mediates Recognition and Phagocytosis of Apoptotic Cells. Nature 1998, 392, 505, DOI: 10.1038/33169. [PubMed: 9548256]

(32). Arashiki N; Takakuwa Y Maintenance and Regulation of Asymmetric Phospholipid Distribution in Human Erythrocyte Membranes: Implications for Erythrocyte Functions. Curr. Opin. Hematol. 2017,24(3), 167–172, DOI: 10.1097/moh.0000000000000326. [PubMed: 28118222]

(33). Boas FE; Forman L; Beutler E Phosphatidylserine Exposure and Red Cell Viability in Red Cell Aging and in Hemolytic Anemia. Proc. Natl. Acad. Sci. U.S.A. 1998, 95 (6), 3077–3081, DOI: 10.1073/pnas.95.6.3077. [PubMed: 9501218]

(34). Schrier SL; Zachowski A; Hervé P; Kader J-C; Devaux PF Transmembrane Redistribution of Phospholipids of the Human Red Cell Membrane During Hypotonic Hemolysis. Biochim. Biophys. ActaBiomembr. 1992,7705(1), 170–176, DOI: 10.1016/0005-2736(92)90176-M.

(35). Pivkin IV; Peng Z; Kamiadakis GE; Buffet PA; Dao M; Suresh S Biomechanics of Red Blood Cells in Human Spleen and Consequences for Physiology and Disease. Proc. Natl. Acad. Sci. U.S.A. 2016,113 (28), 7804–7809, DOI: 10.1073/pnas.l606751113. [PubMed: 27354532]

(36). Coker SA; Szczepiorkowski ZM; Siegel AH; Ferrari A; Mambrini G; Anand R; Hartman RD; Benatti L; Dumont LJ A Study of the Pharmacokinetic Properties and the In Vivo Kinetics of Erythrocytes Loaded With Dexamethasone Sodium Phosphate in Healthy Volunteers. Transfusion Medicine Reviews 2018, 32 (2), 102–110, DOI: 10.1016/j.tmry.2017.09.001. [PubMed: 29031409]

(37). Vankayala R; Mac J; Burns JM; Dunn E; Carroll S; Bahena EM; Patel DK; Griffey S; Anvari B Biodistribution and Toxicological Evaluation of Micron- and Nano-Sized Erythrocyte-Derived Optical Particles in Healthy Swiss Webster Mice. Biomater. Sci. 2019, 7, 2123–2133, DOI: 10.1039/C8BM01448E. [PubMed: 30869663]

(38). Wisse E; Braet F; Luo D; De Zanger R; Jans D; Crabbe E; Vermoesen A Structure and Function of Sinusoidal Lining Cells in the Liver. Toxicol. Pathol. 1996, 24 (1), 100–11, DOI: 10.1177/019262339602400114. [PubMed: 8839287]

(39). Hanayama R; Tanaka M; Miwa K; Nagata S Expression of Developmental Endothelial Locus-1 in a Subset of Macrophages for Engulfment of Apoptotic Cells. J. Immunol. 2004, 172 (6), 3876–3882, DOI: DOI 10.4049/jimmunol.l72.6.3876. [PubMed: 15004195]

(40). Hanayama R; Tanaka M; Miwa K; Shinohara A; Iwamatsu A; Nagata S Identification of a Factor That Links Apoptotic Cells to Phagocytes. Nature 2002, 417 (6885), 182–187, DOI: Doi 10.1038/417182a. [PubMed: 12000961]

(41). Andersen MH; Berglund L; Rasmussen JT; Petersen TE Bovine PAS-6/7 Binds Alpha(V)Beta(5) Integrin and Anionic Phospholipids Through Two Domains. Biochemistry 1997, 36 (18), 5441–5446, DOI: Doi 10.1021/Bi963119m. [PubMed: 9154926]

(42). Otzen DE; Blans K; Wang HB; Gilbert GE; Rasmussen JT Lactadherin Binds to Phosphatidylserine-Containing Vesicles in a Two-Step Mechanism Sensitive to Vesicle Size and Composition. Biochimica Et Biophysica Acta-Biomembranes 2012, 1818 (4), 1019–1027, DOI: 10.1016/j.bbamem.2011.08.032.

(43). Lee T-R; Choi M; Kopacz a. M.; Yun S-H; Liu WK; Decuzzi P On the Near-Wall Accumulation of Injectable Particles in the Microcirculation: Smaller is not Better. Sci. Rep. 2013, 3, 2079, DOI: 10.1038/srep02079. [PubMed: 23801070]

(44). Fish MB; Fromen CA; Lopez-Cazares G; Golinski AW; Scott TF; Adili R; Holinstat M; Eniola-Adefeso O Exploring Deformable Particles in Vascular-Targeted Drug Delivery: Softer is Only Sometimes Better. Biomaterials 2017, 124, 169–179, DOI: 10.1016/j.biomaterials.2017.02.002. [PubMed: 28209527]

(45). Fadok VA; Bratton DL; Rose DM; Pearson A; Ezekewitz RA; Henson PM A receptor for Phosphatidylserine-Specific Clearance of Apoptotic Cells. Nature 2000, 405 (6782), 85–90, DOI: 10.1038/35011084. [PubMed: 10811223]

(46). Setty BNY; Betal SG Microvascular Endothelial Cells Express a Phosphatidylserine Receptor: a Functionally Active Receptor for Phosphatidylserine-Positive Erythrocytes. Blood 2008, 111 (2), 905–914, DOI: 10.1182/blood-2007-07-099465. [PubMed: 17911385]

(47). Manodori AB; Barabino GA; Lubin BH; Kuypers FA Adherence of Phosphatidylserine-Exposing Erythrocytes to Endothelial Matrix Thrombospondin. Blood 2000, 95 (4), 1293–1300. [PubMed: 10666202]

(48). Borst O; Abed M; Alesutan I; Towhid ST; Qadri SM; Foller M; Gawaz M; Lang F Dynamic Adhesion of Eryptotic Erythrocytes to Endothelial Cells via CXCL16/SR-PSOX. Am. J. Physiol., Cell Physiol. 2012, 302 (4), C644–51, DOI: 10.1152/ajpcell.00340.2011. [PubMed: 22173866]

(49). Wautier MP; Heron E; Picot J; Colin Y; Hermine O; Wautier JL Red Blood Cell Phosphatidylserine Exposure is Responsible for Increased Erythrocyte Adhesion to Endothelium in Central Retinal Vein Occlusion. J. Thromb. Haemost. 2011, 9 (5), 1049–1055, DOI: 10.1111/j.1538-7836.2011.04251.x. [PubMed: 21362128]

(50). Fens MHAM; van Wijk R; Andringa G; van Rooijen KL; Dijstelbloem HM; Rasmussen JT; de Vooght KMK; Schiffelers RM; Gaillard CAJM; van Solinge WW A role for Activated Endothelial Cells in Red Blood Cell Clearance: Implications for Vasopathology. Haematol. Hematol. J. 2012, 97 (4), 500–508, DOI: 10.3324/haematol.2011.048694.

(51). Sumpio BE; Riley JT; Dardik A Cells in Focus: Endothelial Cell. Int. J. Biochem. Cell Biol. 2002, 34 (12), 1508–1512, DOI: 10.1016/S1357-2725(02)00075-4. [PubMed: 12379270]

(52). Weis SM; Cheresh DA Pathophysiological Consequences of Vegf-Induced Vascular Permeability. Nature 2005, 437 (7058), 497–504, DOI: 10.1038/nature03987. [PubMed: 16177780]

(53). Roberts WG; Palade GE Increased Microvascular Permeability and Endothelial Fenestration Induced by Vascular Endothelial Growth-Factor. J. Cell Sci. 1995,108, 2369–2379. [PubMed: 7673356]

(54). Ferrara N; Gerber HP; LeCouter J The Biology of VEGF and its Receptors. Nat. Med. 2003, 9 (6), 669–676, DOI: Doi 10.1038/Nm0603-669. [PubMed: 12778165]

(55). Dejana E Endothelial Cell-Cell Junctions: Happy Together. Nat. Rev. Mol. Cell Biol. 2004, 5 (4), 261–270, DOI: 10.1038/nrml357. [PubMed: 15071551]

(56). Long YM; Zhao XC; Clermont AC; Zhou QF; Liu Q; Feener EP; Yan B; Jiang GB Negatively Charged Silver Nanoparticles Cause Retinal Vascular Permeability by Activating Plasma Contact System and Disrupting Adherens Junction. Nanotoxicology 2016,10 (4), 501–511, DOI: 10.3109/17435390.2015.1088589. [PubMed: 26399585]

(57). Setyawati MI; Tay CY; Chia SL; Goh SL; Fang W; Neo MJ; Chong HC; Tan SM; Loo SCJ; Ng KW; Xie JP; Ong CN; Tan NS; Leong DT Titanium Dioxide Nanomaterials Cause Endothelial Cell Leakiness by Disrupting the Homophilic Interaction of Ve-Cadherin. Nat. Commun. 2013, 4, 1673,DOI: 10.1038/Ncomms2655. [PubMed: 23575677]

(58). Reid M; Takakuwa Y; Conboy J; Tchernia G; Mohandas N Glycophorin C Content of Human Erythrocyte Membrane is Regulated by Protein 4.1. Blood 1990, 75 (11), 2229–2234. [PubMed: 2346783]

(59). Nicolas V; Le Van Kim C; Gane P; Birkenmeier C; Cartron J-P; Colin Y; Mouro-Chanteloup I Rh-RhAG/Ankyrin-R, a New Interaction Site between the Membrane Bilayer and the Red Cell Skeleton, is Impaired by Rhnull-associated Mutation. J. Biol. Chem. 2003, 278 (28), 25526–25533, DOI: 10.1074/jbc.M302816200.

(60). Manno S; Takakuwa Y; Mohandas N Identification of a Functional Role for Lipid Asymmetry in Biological Membranes: Phosphatidylserine-Skeletal Protein Interactions Modulate Membrane Stability. Proc. Natl. Acad. Sci. U.S.A. 2002, 99 (4), 1943–1948, DOI: 10.1073/pnas.042688399. [PubMed: 11830646]

(61). Johnson CP; Tang H-Y; Carag C; Speicher DW; Discher DE Forced Unfolding of Proteins Within Cells. Science 2007, 317 (5838), 663–666, DOI: 10.1126/science.1139857. [PubMed: 17673662]

(62). Safeukui I; Buffet PA; Perrot S; Sauvanet A; Aussilhou B; Dokmak S; Couvelard A ; Hatem DC; Mohandas N; David PH; Mercereau-Puijalon O; Milon G Surface Area Loss and Increased Sphericity Account for the Splenic Entrapment of Subpopulations of Plasmodium falciparum Ring-Infected Erythrocytes. PLoS One 2013, 8 (3), e60150, DOI: 10.1371/joumal.pone.0060150.

(63). Lu T; Mac JT; Tweini R; Tran K; Vankayala R; Anvari B Mechanical Characterization of Erythrocyte-Derived Optical Microparticles by Quantitative Phase Imaging and Optical Tweezers, SPIE: 2019; Vol. 10887, Quantitative Phase Imaging V, Proc. SPIE,.

(64). Cokelet GR; Meiselman HJ Rheological Comparison of Hemoglobin Solutions and Erythrocyte Suspensions. Science 1968,162 (3850), 275–277, DOI: 10.1126/science.162.3850.275. [PubMed: 5675469]

(65). Mohandas N; Chasis JA Red Blood Cell Deformability, Membrane Material Properties and Shape: Regulation by Transmembrane, Skeletal and Cytosolic Proteins and Lipids. Semin. Hematol. 1993,30(3), 171–192. [PubMed: 8211222]

(66). Baumler H; Neu B; Donath E; Kiesewetter H Basic Phenomena of Red Blood Cell Rouleaux Formation. Biorheology 1999, 36 (5–6), 439–42. [PubMed: 10818642]

(67). Weisel JW; Litvinov RI Red Blood Cells: the Forgotten Player in Hemostasis and Thrombosis. J. Thromb. Haemost. 2019,17 (2), 271–282, DOI: doi:10.1111/jth.14360. [PubMed: 30618125]

(68). Baumler H; Neu B; Mitlohner R; Georgieva R; Meiselman HJ; Kiesewetter H Electrophoretic and Aggregation Behavior of Bovine, Horse and Human Red Blood Cells in Plasma and in Polymer Solutions. Biorheology 2001, 38 (1), 39–51. [PubMed: 11381164]

(69). Jacques SL Optical Properties of Biological Tissues: a Review. Phys. Med. Biol. 2013, 58 (11), R37–R61, DOI: 10.1088/0031-9155/58/11/r37. [PubMed: 23666068]

(70). Burns JM; Jia W; Nelson JS; Majaron B; Anvari B Photothermal Treatment of Port-Wine Stains Using Erythrocyte-Derived Particles Doped with Indocyanine Green: a Theoretical Study. J.Biomed. Opt. 2018,23(12), 121616, DOI: 10.1117/1.Jbo.23.12.121616.

(71). Moy AJ; White SM; Indrawan ES; Lotfi J; Nudelman MJ; Costantini SJ; Agarwal N; Jia W; Kelly KM; Sorg BS; Choi B Wide-Field Functional Imaging of Blood Flow and Hemoglobin Oxygen Saturation in the Rodent Dorsal Window Chamber. Microvasc. Res. 2011,82 (3), 199–209. [PubMed: 21787792]

(72). Menger MD; Laschke MW; Vollmar B Viewing the Microcirculation Through the Window: Some Twenty Years Experience with the Hamster Dorsal Skinfold Chamber. Eur. Surg. Res. 2002, 34 (1–2), 83–91. [PubMed: 11867907]

(73). Choi B; Jia W; Channual J; Kelly KM; Lotfi J The Importance of Long-Term Monitoring to Evaluate the Microvascular Response to Light-Based Therapies. J. Invest. Dermatol. 2008,128 (2), 485–488. [PubMed: 17657245]

(74). Sato Y; Nakajima S; Shiraga N; Atsumi H; Yoshida S; Koller T; Gerig G; Kikinis R Three-Dimensional Multi-Scale Line Filter for Segmentation and Visualization of Curvilinear Structures in Medical Images. Medlmage Anal 1998, 2 (2), 143–68.

(75). Dunn AK; Bolay T; Moskowitz MA; Boas DA Dynamic Imaging of Cerebral Blood Flow Using Laser Speckle. J. Cereb. Blood Flow Metab. 2001, 21 (3), 195–201, DOI: Doi 10.1097/00004647-200103000-00002. [PubMed: 11295873]

(76). Ramirez-San-Juan JC; Ramos-Garcia R; Guizar-Iturbide I; Martinez-Niconoff G; Choi B Impact of Velocity Distribution Assumption on Simplified Laser Speckle Imaging Equation. Opt. Express 2008, 16(5), 3197–3203, DOI: Doi 10.1364/0e.16.003197. [PubMed: 18542407]

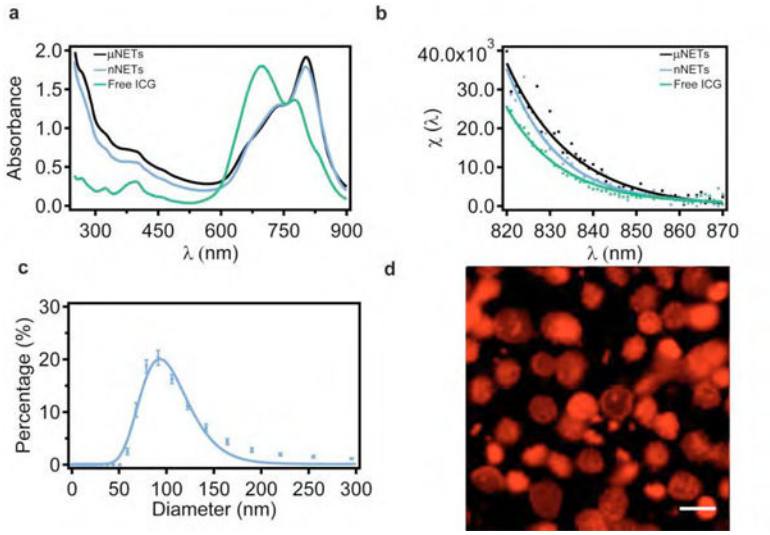

Figure 1.

Characterization of NETs. (a) Absorption and (b) fluorescence emission intensity divided by the quantity of the absorbed light (see Equation 1) for μNETs, nNETs and 18 μM free ICG in 310 mOsm PBS and in response to 785±2.5 nm excitation, (c) Hydrodynamic diameter distribution of nNETs suspended in 310 mOsm PBS as estimated by dynamic light scattering (DLS). The mean and standard deviation of the measurements (n = 4) are represented as circles and error bars, respectively. The estimated mean value of the peak diameter as determined from the lognormal fits (solid curves) is ~ 93 nm. (d) Fluorescence image of μNETs obtained by confocal microscopy. NIR emission is falsely colored in red. Scale bar corresponds to 5 μm. NETs were fabricated from bovine erythrocytes.

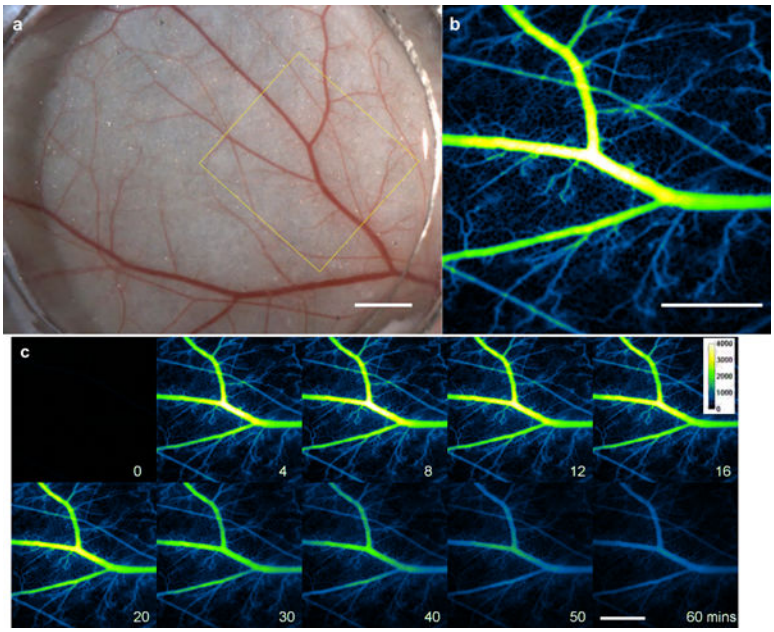

Figure 2.

Intravital imaging of mouse skin microvasculature in window chamber. (a) Representative bright-field image and (b) its corresponding NIR fluorescent image at 6 minutes post μNETs administration. (c) Montage demonstrating the dynamic changes in fluorescence intensity in the vasculature over the 60 minutes imaging period after μNETs administration. White bars in Panels a, b and c represent 1 mm. White bar on the 60 mins panel applies to all images shown in Panel C. NIR images are falsely-colored. NETs were fabricated from bovine erythrocytes.

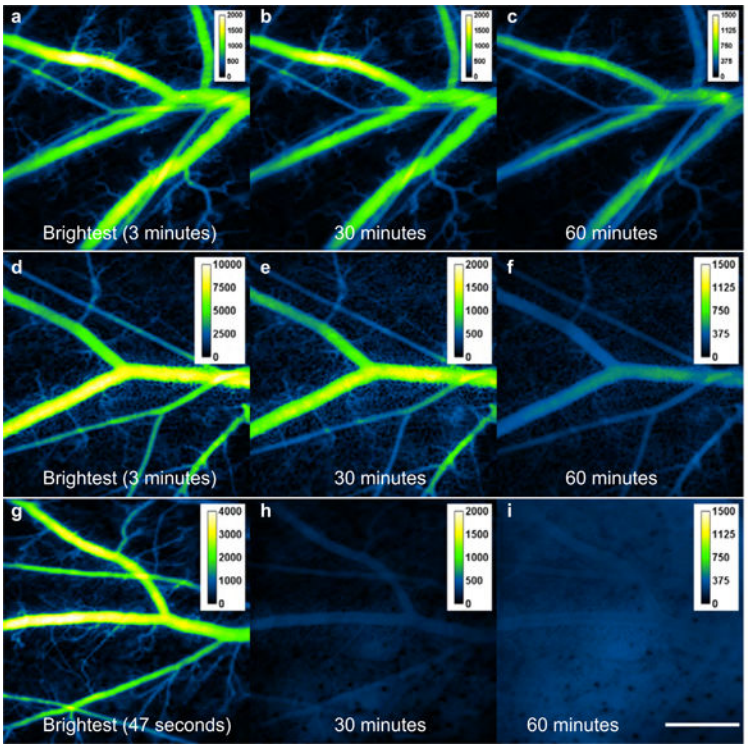

Figure 3.

Intravital NIR fluorescent images of mouse skin microvasculature in the window chamber after single injection of NETs, or free ICG. (a-c) μNETs, (d-f) nNETs, and (g-i) free ICG. Note that the scales in Panels a, d, g are different from each other. Panels a, d, and g correspond to the time at which the highest mean emission from blood vessels were observed for μNETs, nNETs, and free ICG, respectively. White bar shown on panel i represents 1 mm, and applies to all images. NIR images are falsely-colored. NETs were fabricated from bovine erythrocytes.

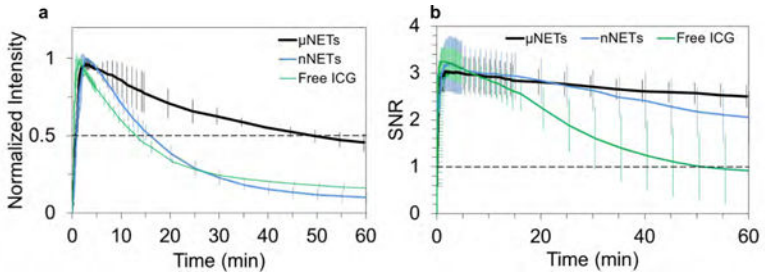

Figure 4.

Quantiative fluorescence dynamics in response to a single injection of NETs or free ICG. Temporal characteristics of (a) normalized fluorescence intensity and (b) SNR (see Equation 2) in the blood vessels after single injection of NETs or free ICG. Each trace is the average of three experiments. Error bars represent the standard deviations from the mean values. NETs were fabricated from bovine erythrocytes.

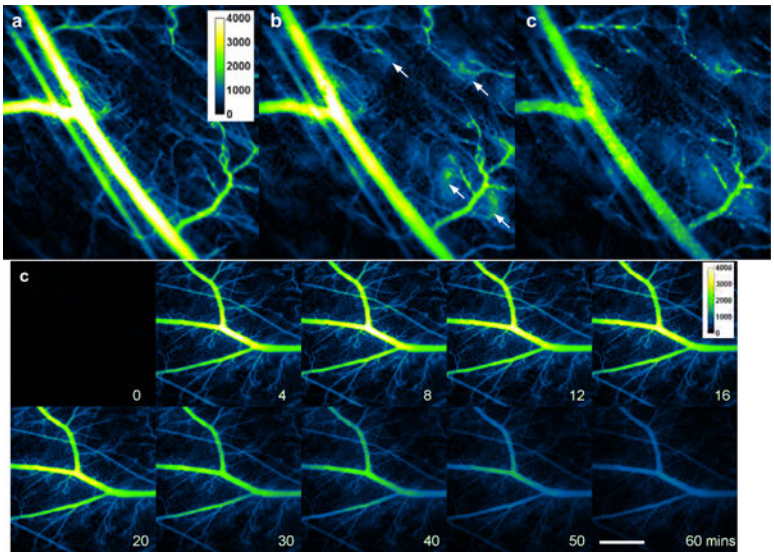

Figure 5.

Intravital NIR fluorescent images of mouse skin microvasculature in the window chamber in response to second injection of μNETs (7 days after first injection), (a-d) Fluorescent images acquired at 3, 13, 30, and 60 minutes for one mouse. (e-f) Fluorescent images at 12 and 10 minutes post-injection, respectively, for a second and third mouse. In Panels (b), (e) and (f), bright spots are visible in the regions around the tips of the capillaries (white arrows). In Panels (c) and (d), there are large and bright particles on the vessel wall. White bar represents 1 mm and applies to all panels. NIR images are falsely-colored. NETs were fabricated from bovine erythrocytes.

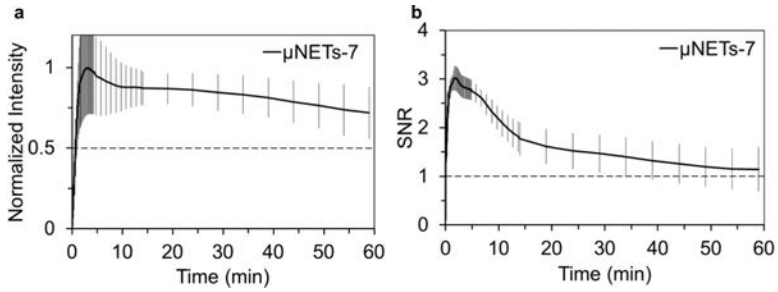

Figure 6.

Quantiative fluorescence dynamics in response to the second injection of μNETs (designated as μNETs-7) seven days after the first injection. Temporal characteristics of (a) normalized fluorescence intensity and (b) SNR (see Equation 2) in the blood vessels after the second injection of μNETs. Each trace is an average of four experiments. Error bars represent the standard deviations from the mean values. NETs were fabricated from bovine erythrocytes.

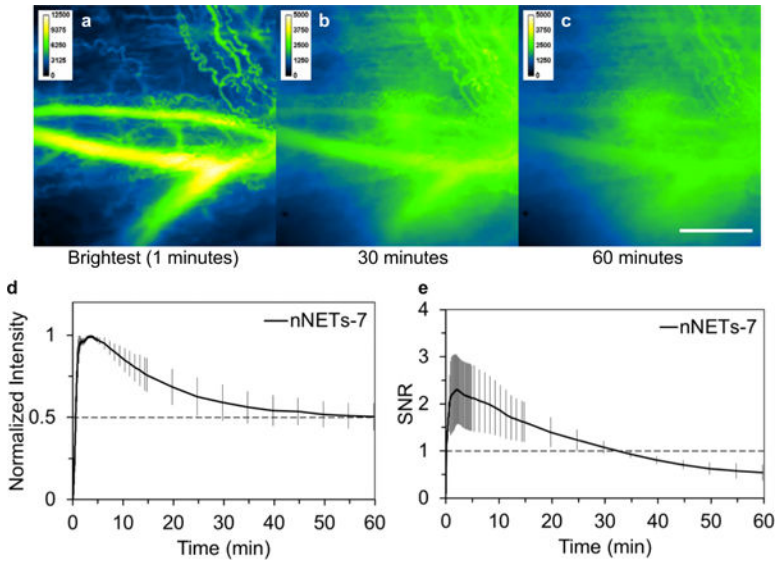

Figure 7.

Intravital NIR fluorescent images of the microvasculature in the window chamber and quantiative fluorescence dynamics in response to second injection of nNETs (designated as nNETs-7). (a-c) Fluorescent images at one minute (time of maximum emission intensity), 30 and 60 minutes after second injection. Note that background tissue fluorescence intensity at 30 and 60 minutes after injection is quite high (Panels b, c). White bar in panel c represents 1 mm, and applies to all images. NIR images are falsely-colored. Temporal characteristics of (d) normalized fluorescence intensity and (e) SNR (see Equation 2) in the blood vessels after the second injection of nNETs. Each trace is the average of three experiments. Error bars represent the standard deviations from the mean values. NETs were fabricated from bovine erythrocytes.

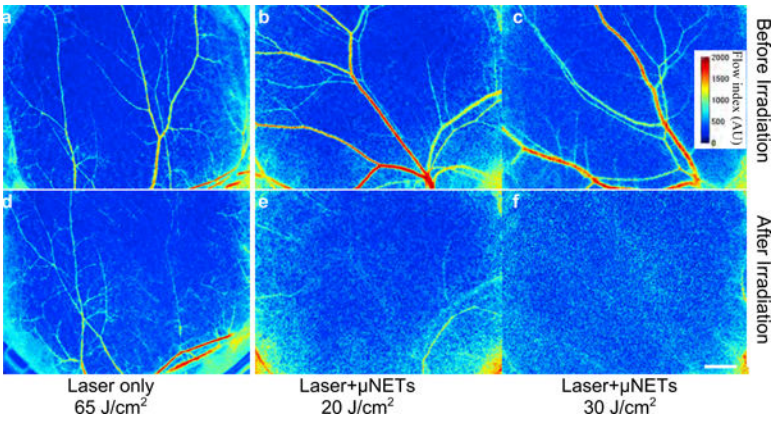

Figure 8.

Blood flow maps of skin microvasculature within the window chamber obtained by laser speckle contrast (LSC) imaging, (a-c) Before, and (d-f) ~5 minutes after 755 nm laser irradiation at various fluences without (d) or with (e, f) administration of μNETS. Laser pulse duration and spot size were 3 ms, and 10 mm, respectively. White bar represents 1 mm and applies to all images. Images are falsely-colored. NETs were fabricated from bovine erythrocytes.

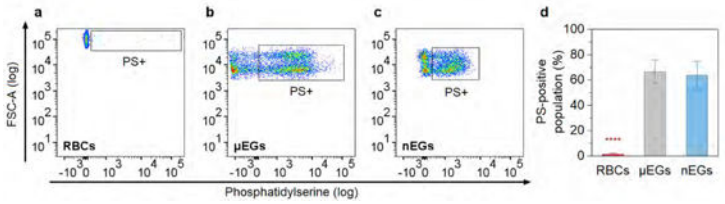

Figure 9.

PS quantification for RBCs, μEGs, and nEGs as determined by flow cytometry. (a-c) Representative dot plots of forward scattering vs. fluorescence emission of Alexa Fluor 488-labeled annexin V to target PS on RBCs, μEGs, and nEGs. Boxed regions correspond to PS-positive RBCs and EGs. (d) Mean fraction of PS-positive RBCs, μEGs, and nEGs populations. Error bars represent one standard deviation from the mean (n=3 samples for each indicated material). **** indicates statistically difference (p <0.0001) between the mean value for RBCs vs those for μEGs and nEGs. Note that some fraction of nEGs may have been too small to be detected and do not appear on the dot plot.